Zahn, R., Comas, M.C., and Klaus, A. (Eds.), 1999
Proceedings of the Ocean Drilling Program, Scientific Results, Vol. 161

7. DESCRIPTION, CLASSIFICATION, AND ORIGIN OF UPPER PLIOCENE–HOLOCENE MARINE SEDIMENTS IN THE ALBORAN BASIN[1]

C.G. Skilbeck[2] and J.S. Tribble[3]

ABSTRACT

Upper Pliocene–Holocene deep marine sediments from four sites in the Alboran Basin drilled during Ocean Drilling Program Leg 161 are remarkably uniform in their overall composition and texture despite the geographic isolation of the sites. The sediments are predominantly structureless to burrowed clays and silty clays, in which the main components are calcareous nannofossils, clay, and sand-sized foraminifers. Quartz and feldspar of detrital origin form a minor common fraction. One hundred and sixty samples were analyzed by wet sieving for grain-size distribution and by X-ray diffraction for mineralogy. The textural data confirm visual descriptions of the shipboard scientists, and all samples contain over 87% clay and fine silt (<20-µm grain-size diameter) and, on average, only 3%–4% sand. The proportions of a suite of 14 minerals (quartz, albite, bytownite, orthoclase, chlorite, illite, kaolinite, muscovite, talc, halite, pyrite, gypsum, dolomite, and calcite) were quantified using Siroquant software, and the results confirm the dominant carbonate composition. Downhole distribution of the proportions of quartz, which was used to infer detrital input, "clay" (all phyllosilicate minerals regardless of origin), and total carbonate (calcite + dolomite) for each of the four holes examined are variable and broadly cyclic, but show no clear trends when compared either with each other or with sedimentation rate. Between-hole temporal correlation of cycles in both the <20-µm carbonate fraction (nannofossils) and the >63-µm carbonate fraction (foraminifers) is reasonably strong at frequencies of ~500 ka for the former and 750 ka for the latter. This suggests a regional control on carbonate deposition, which is interpreted to most probably be climatic in origin. In contrast, cycles in quartz distribution cannot be regionally correlated for any of the grain-size fractions, and sources cannot be unequivocally resolved. However, we propose that the detrital material has been deposited by a combination of gravity current and eolian processes, and then mixed with pelagic and benthic components.

INTRODUCTION

Upper Pliocene–Holocene sediments present in cores recovered from western Mediterranean Ocean Drilling Program Sites 976, 977, 978, and 979 (Fig. 1) are dominated by poorly sorted, structureless to bioturbated marine clay and silty clay. Microfossils and sedimentary character indicate that these sediments were deposited continuously throughout the last ~3.9 m.y. Uncorrected average sediment accumulation rates calculated from nannofossil biostratigraphy range from ~120 to 200 m/m.y. during the Pleistocene–Holocene and from ~100 to 350 m/m.y. for the late Pliocene (Comas, Zahn, Klaus, et al., 1996). Composition of this dominant sediment includes a carbonate fraction, composed mainly of silt-sized nannofossils, and a siliceous fraction, suggested by shipboard scientists to comprise mainly clay minerals. Importantly, the siliceous fraction of the clay and silty clay also includes up to 15% (Shipboard Scientific Party, 1996b, fig. 25) silt- to sand-sized quartz, feldspar, and detrital mica, and rarer garnet, zircon, and sedimentary and metamorphic rock fragments. The presence of terrigenous detrital material in the marine sediment is not surprising, given the relative proximity of the elevated continental hinterland surrounding the Alboran Sea and the provenance of sediment being delivered to the shoreline (Stanley et al., 1975). The mode of (and possible controls on) transport and deposition of these sediments in the marine realm, however, is not clear, mainly because primary depositional sedimentary structures are absent from most of the recovered sequence. A wide variety of volumetrically insignificant sediment types is present throughout the upper Pliocene–Holocene section, and these sediments provide clues about the style of sedimentation, but do not account totally for the majority of the sediment.

In this paper we aim to test the hypotheses of shipboard scientists (Shipboard Scientific Party, 1996b; Skilbeck et al., 1995) about transport mechanisms and controls and about supply cyclicity for the terrigenous clastic component of the sediment. Most of the carbonate material is pelagic in origin, comprising mainly foraminifers and nannofossils, but may have been reworked after initial deposition. Given the open marine setting indicated by the fossil assemblage, the mode of transport and deposition of the detrital siliciclastic material is more enigmatic and may be partly dependent on the grain size of this material. One possible scenario is that the clay and fine silt-sized quartz and feldspar had either a hemipelagic-suspension or a wind-blown origin, whereas coarser silt and sand-sized material could suggest transport by gravity currents. Basin-wide cyclic trends in grain-size variation could have tectonic and/or climatic implications.

As a preliminary part of this study, we have undertaken a more precise and objective quantification of textural and compositional data that were determined visually by shipboard scientists to confirm their estimates of these parameters.

Although lower Pliocene sediments were recovered at all four Alboran sites and Miocene sediments at three of the four Leg 161 sites (Sites 976, 977, and 978), our study is confined to upper Pliocene and overlying material because the older section is punctuated by unconformities that involve removal of unknown thicknesses of sediment. This renders meaningful correlation of sedimentation rates impossible.

UPPER PLIOCENE–HOLOCENE STRATIGRAPHY

An upper Pliocene–Holocene section is present at each of the four Alboran Sea sites drilled during Leg 161 (Fig. 1) and, at the resolution of micropaleontological sampling, each appears to have been deposited without significant nondepositional or erosional breaks. The dominant sediment type present in the studied interval of all sites is gray to green nannofossil clay and silty clay (see Shipboard Scientific Party, 1996a, for lithologic classification), which is variously struc-

[1]Zahn, R., Comas, M.C., and Klaus, A. (Eds.), 1999. *Proc. ODP, Sci. Results*, 161: College Station, TX (Ocean Drilling Program).
[2]Department of Applied Geology, University of Technology, Sydney, Australia. G.Skilbeck@uts.edu.au
[3]Department of Oceanography, University of Hawaii, 1000 Pope Road, Honolulu, HI 96822, U.S.A.

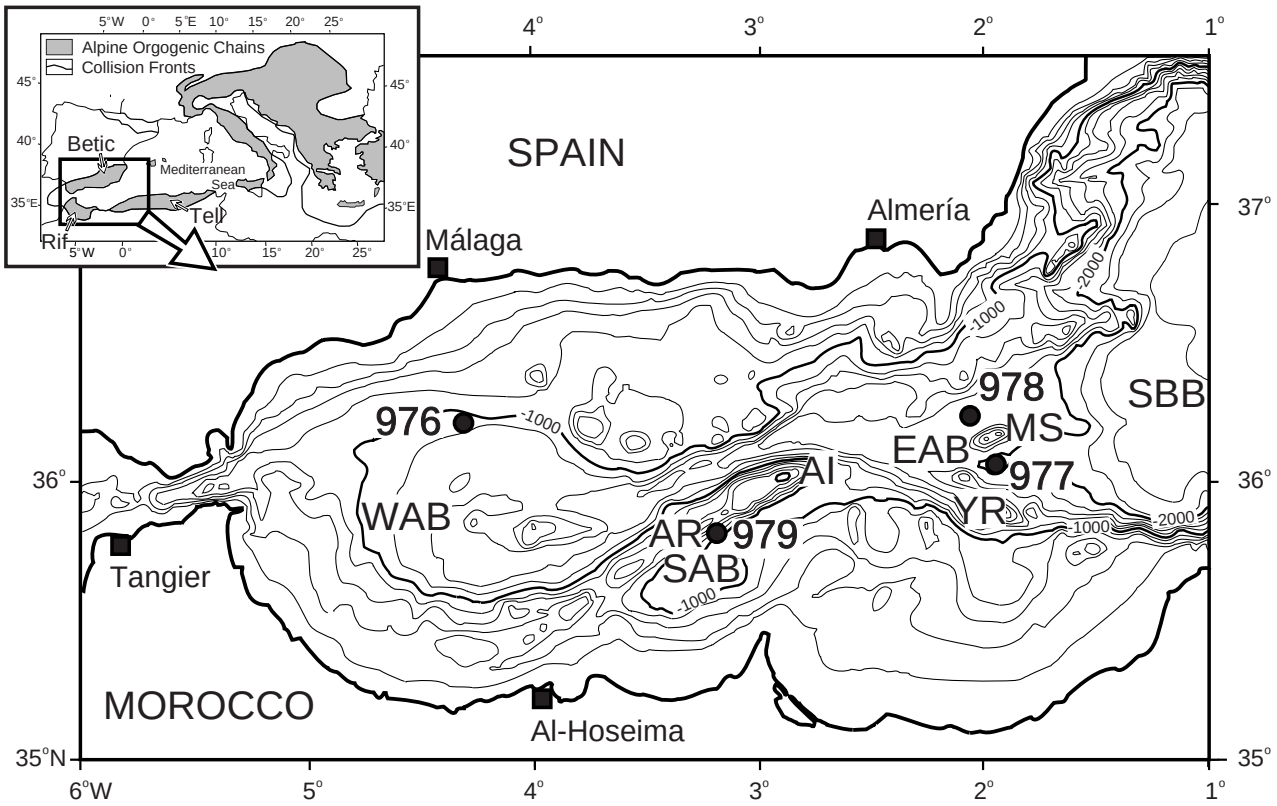

Figure 1. Bathymetric map of the Alboran Sea showing Leg 161 Sites 976, 977, 978, and 979, the location of major basement features, and surrounding clastic source terrains (Rif, Betic, and Tell Cordilleras). Contours in meters, contour interval is 200 m. AI = Alboran Island, AR = Alboran Ridge, EAB = East Alboran Basin, MS = Al-Mansour Seamount, SAB = South Alboran Basin, SBB = South Balearic Basin, WAB = Western Alboran Basin, YR = Yusuf Ridge.

tureless, mottled, or burrowed. Several subordinate lithotypes are present, and these impart a variable stratigraphy, discussed below, across the Alboran Basin. The variations are at least in part caused by local influences at the widely spaced sites.

A continuous section from the seafloor to below the upper/lower Pliocene boundary was cored at Sites 976 and 977. At Site 978 the uppermost 213 m below seafloor (mbsf) was drilled without coring except for two 9-m spot cores, but the hole did penetrate the upper/lower Pliocene boundary. At Site 979, the section was cored from the seafloor and drilling was terminated in sediments of late Pliocene age. The stratigraphy of the studied intervals is given in Figure 2. Organic-rich layers (ORLs) are present in the Pleistocene–Holocene interval at Sites 976, 977, and 979, and these can be correlated across the Alboran, Balearic, and Tyrrhenian Basins, and across the eastern Mediterranean (see Murat, Chap. 41, this volume). The host sediment for these enriched layers is the nannofossil clay and silty clay that is the subject of this study, but the description, interpretation, and significance of the ORLs themselves are discussed in Murat (Chap. 41, this volume).

Site 976 (Western Alboran Sub-Basin)

Five holes were drilled at Site 976. Of these, only Hole 976B continuously cored from the seafloor to beneath the base of the upper Pliocene. Hole 976C, offset 50 m to the east of Hole 976B, cored most of the section from the seafloor, but was terminated above the base of the upper Pliocene. The stratigraphic section intersected by the two holes correlates well, there being no significant difference between the studied intervals (Fig. 2). Only samples collected from Hole 976B were available for this study.

At Site 976, the upper Pliocene–Holocene section is divided into two parts (Fig. 2), an upper nannofossil clay- and silty clay-dominated unit (lithostratigraphic Unit I, 0–362.1 mbsf) and a lower unit (lithostratigraphic Unit II), which is present between 362.1 and 518.3 mbsf. Core recovery from Unit II was low (17 m of the 142 m drilled, ~12%; Shipboard Scientific Party, 1996b). However, the described sediment types include sand- and silt-dominated beds present as discrete layers interstratified with nannofossil clay and silty clay. The sub-sand–grade sediment is indistinguishable from that in Unit I in texture and mineral composition. At least 22% of Unit II comprises sand or silt beds of this type (Shipboard Scientific Party, 1996b, p. 189). Hole 976B continued to a depth of 928.7 mbsf, where it was terminated in metamorphic basement. Hole 976C penetrated all of Unit I (362.8 m) and ~17 m of Unit II.

In Hole 976B, the Pliocene/Pleistocene boundary is located near the base of lithostratigraphic Unit I in the interval 357.9–361 mbsf. Unit II is entirely late Pliocene in age, lying unconformably over lower Pliocene marine clay. The oldest late Pliocene fauna present in Unit II comprises nannofossil zone NN18 (Shipboard Scientific Party, 1996b, p.201), four zones above the upper/lower Pliocene boundary.

Layering of two types is present within the dominant nannofossil clay and silty clay of lithostratigraphic Unit I. It is defined either by subtle color alternations or by horizontal to slightly inclined burrows

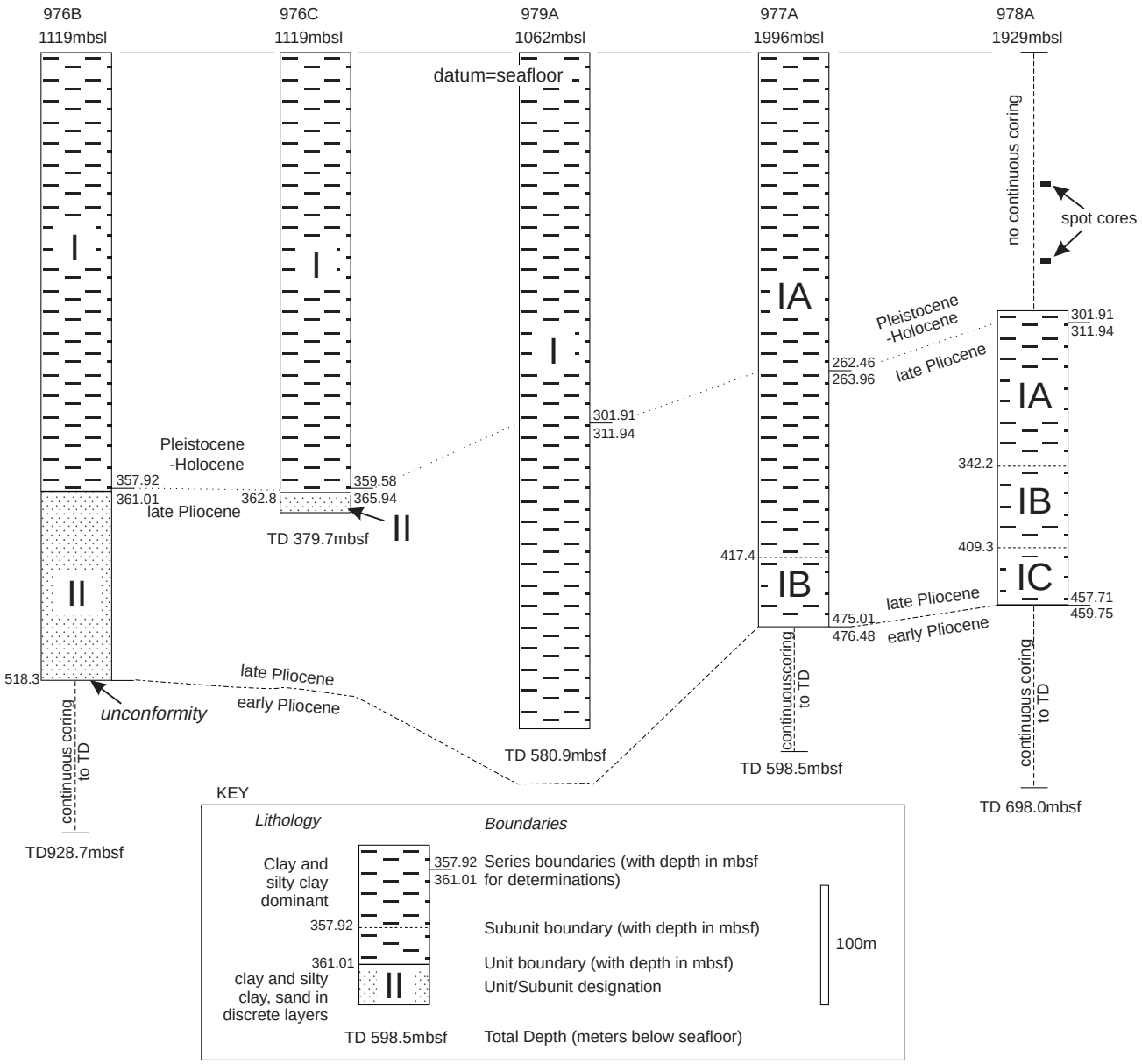

Figure 2. Upper Pliocene–Holocene stratigraphy in the Leg 161 holes referred to in this study. Note that the subdivisions indicated are those that were used by shipboard scientists to describe the sequence at each site and do not indicate time or facies equivalence.

(Fig. 3). At some locations (see Shipboard Scientific Party, 1996b, table 3), color banding can be attributed to a slight enrichment in organic matter that formed a recognized ORL, but this is not the case everywhere. The origin of many color bands remains unknown. Rare subordinate lithologies present in Unit I include silt laminae enriched in pyrite and shell fragments.

Site 977 (Eastern Alboran Sub-Basin)

One fully cored hole, Hole 977A, was drilled at this site. The upper Pliocene–Holocene section is ~475 m thick, and sedimentation was continuous from the early Pliocene (NN14) until the Holocene (Shipboard Scientific Party, 1996c, p. 309). The lower/upper Pliocene boundary is located at 475–476.7 mbsf, and the Pleistocene/Pliocene boundary is between 262 and 264 mbsf.

The interval included in this study lies entirely within lithostratigraphic Unit I, which is dominated by structureless to moderately bioturbated nannofossil and calcareous clay and silty clay. Unit I was divided into three subunits by shipboard scientists (Shipboard Scientific Party, 1996c, fig. 5), and the upper two of these encompass the section included in this study. Prominent millimeter- to centimeter-scale color bands and intense bioturbation characterize the lower Subunit IB, with the color banding indicating alternations of calcareous and nannofossil clay (Shipboard Scientific Party, 1996c, p. 305). Common folded and dismembered intervals of color-banded units that are contemporaneous with confining strata indicate intraforma-

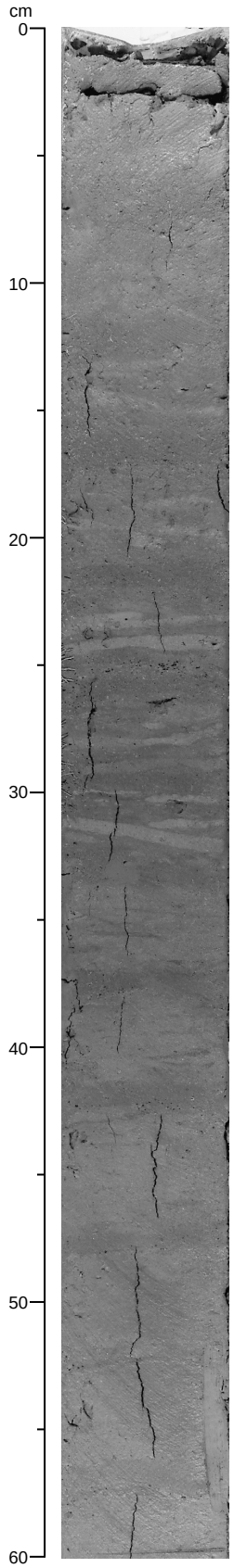

Figure 3. Layering in nannofossil clay produced by horizontal burrows of *Zoophycus* (prominent at 31 and 24 cm; Sample 161-976B-35X-5, 0–60 cm). Note core biscuiting at 4- to 5-cm spacing below 33 cm.

tional slumping and mean that discontinuities within the sequence are possible. In the overlying Subunit IA, the dominant clay and silty clay is characterized by commonly interstratified sand laminae and thin beds of both bioclastic and mixed bioclastic-siliciclastic composition, and by ORLs. Visible bioturbation in the clay and silty clay is moderate to slight when compared with Subunit IB, and soft-sediment deformation is rare. The gradational boundary between the two subunits is placed at 417.4 mbsf.

Site 978 (Eastern Alboran Sub-Basin)

Three stratigraphic divisions are recognized within the sedimentary interval cored at Site 978. The single hole, Hole 978A, was drilled without continuous coring to a depth of 213 mbsf and was then fully cored to total depth at 698 mbsf. Two 9-m spot cores were taken from the upper part of the hole; from 110.3 to 119.9 mbsf and from 168.4 to 178.0 mbsf. The section is late Pliocene–Pleistocene in age and is contained wholly within lithostratigraphic Unit I. Sedimentation was continuous across both the upper/lower Pliocene boundary, which is located between 457.7 and 459.8 mbsf, and the upper Pliocene/Pleistocene boundary, which is present in the interval between 222.8 and 223.4 mbsf.

Lithostratigraphic Unit I was divided into three subunits designated IA, IB, and IC from the seafloor downwards, with the late/early Pliocene boundary located in the lowermost Subunit IC. Variably bioturbated nannofossil clay and silty clay are the principal sediment types present in Unit I. Stratification, where present, is defined by decimeter-scale “dark” and “light” color bands, in which some examples of the former have a silty lower interval up to 10 cm thick, overlying a sharp basal contact (Shipboard Scientific Party, 1996d, p. 357). Color banding was determined shipboard to be a function of carbonate content, with the darker bands having less than the lighter bands in any one sequence. The division into subunits is based mainly on details of sedimentary features observed within the color bands, and also on Subunit IC being considered sufficiently lithified to be called a claystone (see Shipboard Scientific Party, 1996a, for lithologic distinction). Minor calcareous (shell debris and foraminifer tests) and mixed calc-siliciclastic sand and silty sand layers are present throughout the interval studied. ORLs are assumed to have been present in the noncored upper section of the hole.

Site 979 (Southern Alboran Basin)

A single fully cored hole, Hole 979A, was drilled at this site and reached a total depth of 580.9 mbsf in upper Pliocene (NN16A) marine clayey sediment. All nannofossil zones younger than this are present in the hole, which supports continuous sedimentation. The late Pliocene/Pleistocene boundary is located in the interval 341–345 mbsf (Shipboard Scientific Party, 1996e, p. 397). The stratigraphic section was remarkably uniform in lithologic character at this locality, and only one stratigraphic unit, designated lithostratigraphic Unit I, was established. The predominant lithology is nannofossil clay, which is commonly burrowed. ORLs, in which nannofossil clay is the host sediment, are confined to the Pleistocene section (Shipboard Scientific Party, 1996e, table 2), as are most of the diatom-bearing intervals. Discrete sand and silt layers (Shipboard Scientific Party, 1996e, table 3) are regularly present throughout the entire section.

SEDIMENT PETROGRAPHY

The main sediment type comprising the upper Pliocene–Holocene stratigraphy of the deep marine Alboran Sea is nannofossil clay to silty clay that contains a wide variety of subsidiary minerals and a range of particle sizes. On the basis of shipboard visual estimates of the component proportions from smear-slide analyses, a typical tex-

ture is 88% clay-sized, 10% silt-sized, and 2% sand-sized, and a typical mineralogy is 51% clay minerals, 30% nannofossils, 6% quartz, 5% other carbonate (bioclasts, dolomite, foraminifers, micrite), 4% siliceous organic material (diatoms and sponge spicules), and 2%–3% other detrital silicate minerals (feldspar, mica, opaque minerals) and rock fragments (Sample 161-979A-20X-4, 54–55 cm).

The nannofossil clay and silty clay from all sites is poorly to moderately sorted, with particles ranging from clay (<4 µm) to sand size (>63 µm). The clay and fine silt sizes dominate, but coarse silt and sand are present everywhere. In some samples, sand-sized material was estimated to make up more than 20% of the clay/silty clay. In many cores, identifiable trace fossils are present, and poor sorting can most probably be attributed to biological mixing. However, a significant part of the sediment is either structureless (Fig. 4) or displays only an indistinct wispy or mottled structure.

From the typical composition cited above, it can be seen that the main sediment type comprises (1) a carbonate component, principally calcareous nannofossils, but also with foraminifers, shell fragments and other bioclasts, micrite, and some inorganic calcite and dolomite, and (2) a siliceous component, which the shipboard scientists determined is mainly clay minerals, but commonly includes quartz, feldspar, glauconite, muscovite, opaque minerals and rock fragments, and relatively rare diatom tests and siliceous sponge spicules.

In terms of a relationship between grain size and composition, only a qualitative estimate was made on board ship. In the carbonate fraction, grain-size distribution is a function of taxonomy and preservation state. Nannofossils, the main carbonate component, are confined to the fine silt and clay fraction (>20 µm). Whole foraminifers constitute the majority of the carbonate fraction of sand. Fragments of shells and foraminifers are present in both sand and silt fractions, and may also be present in the clay fraction.

The main siliciclastic components, quartz and feldspar, are commonly present in both sand and silt fractions and may be present in the clay fraction. No estimate of the proportional distribution was made by shipboard scientists, and one of the aims of the present study is to quantify the grain-size distribution of the siliciclastic components.

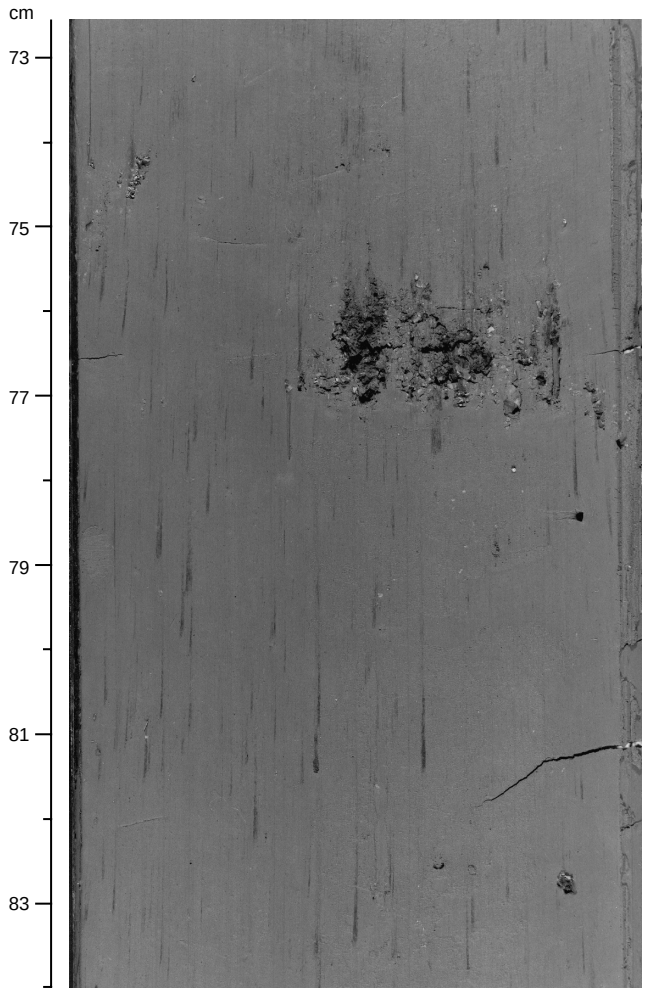

Figure 4. Structureless nannofossil clay showing isolated sandy bleb (Sample 161-976C-4H-4, 72.5–84 cm). Smearing of pyrite blebs up core occurred during core splitting.

SAMPLES AND METHODOLOGY

It was originally intended that the quantification of data would be undertaken mainly by microscope examination and point counting using the smear slides prepared shipboard. However, poor sorting of the sediments and the large proportion of grains less than 30 µm in diameter meant that normal petrographic techniques could not be employed. In addition, as we believed it important to examine the siliciclastic grain-size distribution, core plugs of sediment samples were required. Accordingly, we obtained sediment samples (see below), each of which was split into four subsamples on the basis of grain size. X-ray diffraction (XRD) analysis was used to quantify the mineralogy of the entire sample and of each grain-size split individually. The details of sampling procedure, preparation, and analysis are given below.

Sample Collection

Subsamples of ~3–5 cm^3 (~5–10 g) were obtained from 20 cm^3 samples collected shipboard for microfabric study. Subsampling was undertaken at the University of Hawaii in May 1996. The original 20-cm^3 sample suite had been collected at a rate of one per core from the working-half split and stored in sealed plastic bags at a temperature of ~3°C. The subsample set used in this study was collected using a clean stainless steel spatula and was stored in sealable cylindrical plastic tubes that had previously been oven dried at 60°C, cooled in a desiccator, and weighed. The open tubes were covered with permeable plastic wrap, frozen to –25°C, and freeze dried. After warming to ambient temperature in a desiccator, the tube and sample were weighed to determine sample mass. One hundred and sixty samples were taken to Australia in sealed tubes for the remainder of the study.

Sample Preparation

Sediment texture was determined by wet sieving and weighing of individual sample splits (Table 1, on CD-ROM, back pocket, this volume). Between 2 and 6.5 g of each sample was weighed on glossy paper using a Shimadzu electronic balance, brushed into a 100-ml sealed plastic container, and suspended in ~20–30 ml distilled water by vigorous shaking. Samples were split into four grain-size divisions by wet sieving using three 100-mm-diameter sieves with mesh sizes of 63 µm, 32 µm, and 20 µm, stacked over a l-L glass beaker. This gave four grain-size divisions, >63 µm (sand), 63–32 µm (coarse silt), <32–20 µm (mostly medium silt) and <20 µm (fine silt and clay). Sediment was washed through the sieve stack with additional distilled water as required. Gentle agitation was required to break up some aggregates. The three sieve fractions were oven dried in the sieve at 60°C, retrieved by fine brushing onto glossy paper, placed into previously dried and weighed glass vials, and weighed. The <20-µm fraction was centrifuged at 6000 rpm in a Sorvall Superspeed Centrifuge to reduce water content before oven drying in a previously dried and weighed glass Petrie dish. The <20-µm fraction from Holes 976B and 977A was brushed from the glass Petrie dish onto glossy

paper and then sealed into previously dried and weighed glass vials, before weight determination. Total average recovery from the sieving process by this method was 93.4% for the two holes. For Holes 978A and 979A, the proportion of the <20-µm fraction was determined by weight difference (original sample less [>63 µm] + [63–32 µm] + [32–20 µm] fractions) assuming the above recovery rate, to speed up sample recovery. Sieves were cleaned in a sonic bath after each sample run and then rinsed in distilled water. All glass, plastic, and metal ware were washed and rinsed in distilled water between the splitting of each sample.

XRD Analysis

XRD data were collected using a Siemens D5000 X-ray diffractometer setup in θ-θ configuration and housed at the Microstructural Analysis Unit at the University of Technology, Sydney. The X-ray source was a long-fine focus copper anode tube emitting X-rays at 1.540562 Å for $k\alpha_1$ and 1.544390 Å for $k\alpha_2$. Data measurements were made from 2°2θ to 70°2θ at increments of 0.02°2θ. XRD data were collected for each unsorted sample and for each of the four split fractions. Because of the small sample volume in each grade fraction, all samples were dry sedimented onto 25 × 37.5 mm glass slides, dispersed in distilled water, and dried at 60°C. The >63-µm fractions were ground using a mortar and pestle, before being placed on the glass slides.

Quantification of XRD Data

Mineral proportions were calculated using SIROQUANT, a commercially available MS-Windows program for standardless mineral quantification. The software uses up to 15 operator-selected mineral phases, chosen from an included data bank, to calculate a theoretical XRD intensity profile that is then fitted to the measured profile by refinement of the Rietveld parameters. The majority of samples studied here were analyzed using 13 mineral phases (i.e., quartz, albite, bytownite, orthoclase, chlorite, illite, kaolinite, muscovite, talc, halite, pyrite, dolomite, and calcite). Gypsum was additionally present in a few samples and was added to the control (= task) file for their analysis. These minerals fit most of the major crystal peaks represented on the XRD data, and the presence of most was confirmed from other sources. These were (1) quartz, calcareous microfossils, muscovite, and pyrite, which were chosen because they are visible in smear slides, and dolomite, which was identified shipboard by XRD analysis; (2) feldspars, which were also recognized in smear-slide examination, and albite, bytownite, and orthoclase were chosen as representative of the group; (3) halite, which was included because the sediments were deposited in a marine environment; and (4) the four phyllosilicate minerals, which were selected because of the presence of strong primary peaks in the XRD data that most closely corresponded to standard patterns for these particular minerals. Unoriented hkl files were used for all phases except the clays, for which hkl files oriented on the 001 face and multiples were created and used because of the method of sample preparation.

The above mineral suite was not entirely satisfactory, particularly with respect to the clay minerals, but as these were not the primary focus of the study, refinement of identification was not pursued in this study. The principle difference between samples was the variable d-spacing represented by the peaks between 6°2θ and 13°2θ. In particular, the peak representing a lattice d-spacing of 14.2Å, interpreted to be an oriented 001 chlorite peak, varies between 14.40 and 14.04Å. Similarly the muscovite 002, talc 002, and kaolinite 001 peaks, represented by high intensities at around 8.88°2θ, 9.46°2θ, and 12.46°2θ, respectively, are all interpreted to result from mixed layer structures. The net effect of variable phyllosilicate composition on the SIROQUANT analysis is to increase the χ^2 value to above 3.00. Nevertheless, the mineral percentages generated by SIROQUANT are believed able to indicate meaningful downhole variation for quartz and carbonate material (see below).

Calibration of XRD Data

To check the XRD quantification performed by SIROQUANT, 20 samples were analyzed for weight percent carbon. Organic and inorganic carbon content of the uppermost 20 samples in Hole 976B was determined using a UIC Coulometer housed at the Department of Chemical Engineering, University of Sydney. Chemical data are plotted vs. XRD-determined proportions of calcite + dolomite (Fig. 5) and show a clear linear relationship, with the XRD-determined values being mostly <10% higher than the chemically determined values over the range of carbonate values from 20%–40%. The exceptions are samples 161-976B-1H-2, 64–68 cm (XRD determined carbonate is 17.8% higher than the chemically analyzed sample), and 161-976B-8H-5, 77–80 cm (XRD determined carbonate is 2.16% lower than the chemically analyzed sample). Although SIROQUANT was not able to determine accurate values for the carbonate, of more importance to the aims of this study is its ability to reproduce the downhole trend in the carbonate data (Fig. 6). Unfortunately, accurate quantification of the portion of any crystalline phase during SIROQUANT analysis was not possible. Values reported in this study define downhole trends, and subsequent interpretation of data is based on this.

SEM and EDS Analysis

The >63-µm and <20-µm grain-size splits of four selected samples (161-976B-5H-5, 77–82 cm, 161-976B-10H-3, 76–81 cm, 161-976B-15X-3, 76–80 cm, and 161-976B-20X-3, 95–100 cm) were examined using a Jeol JSM 6300F scanning electron microscope (SEM), so that the shape and rounding of the quartz and feldspar grains could be determined. Of particular interest was the texture of these minerals in the <20-µm grain-size fraction, as this was impor-

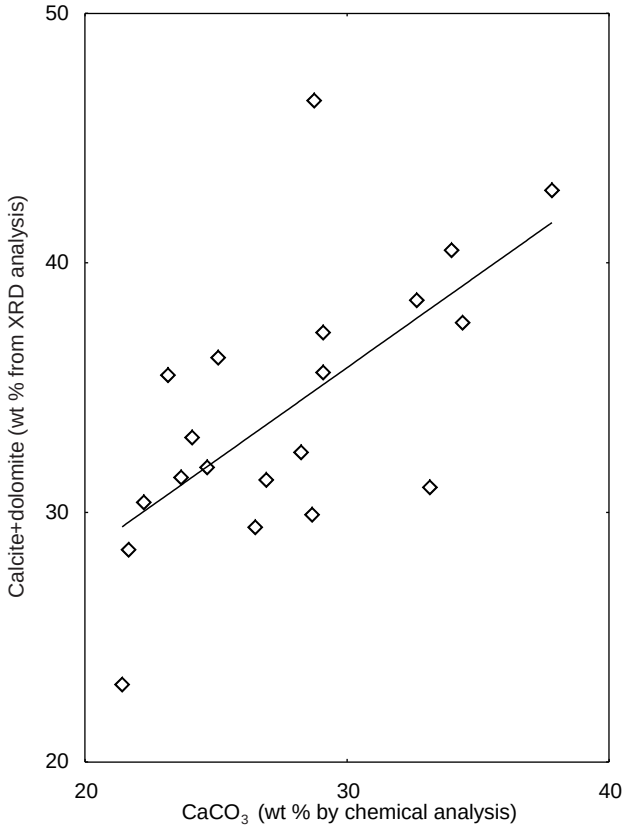

Figure 5. Chemically determined total carbonate content (wt%) plotted vs. XRD-determined calcite + dolomite (from Fig. 6). Correlation coefficient using least-squares linear regression = 0.516.

tant to interpret whether their origin was detrital or authigenic. The SEM was fitted with a Moran Scientific EDS/XRM analyzer that was employed to confirm mineral identification.

Sedimentation Rate

Sedimentation rates based on decompacted sediment thickness were calculated for each pair of sample locations in each hole. Decompacted thicknesses were used in preference to the raw shipboard determinations to enable direct cross-hole correlation of data.

Numeric ages for the calculations were determined from the composite calcareous nannofossil and planktonic foraminiferal biostratigraphic charts given in the preliminary summary of drilling results (Shipboard Scientific Party, 1996b, table 4, for Hole 976B; Shipboard Scientific Party, 1996c, table 5, for Hole 977A; Shipboard Scientific Party, 1996d, table 3, for Hole 978A; and Shipboard Scientific Party, 1996e, table 4 for Hole 979A). Numeric ages for each sample point were calculated by linear interpolation between the mbsf depth/age tie points and are given in Table 2 (on CD-ROM, back pocket, this volume).

Decompacted sediment thicknesses were calculated for each of the mbsf depth/age tie points first using the following relationship determined by Falvey and Middleton (1981):

$$1/\phi = 1/\phi_0 + ky, \quad (1)$$

(where ϕ = porosity at any given depth, ϕ_0 = porosity at 0 depth, y = depth, and k = constant related to lithology), to determine a value for k. For this study k = 0.00154605, which was calculated using the porosity data reported by Comas, Zahn, Klaus, et al. (1996) for Hole 976B (Fig. 7) and ϕ_0 = 0.637. Data for Holes 977A and 979A yield almost identical results.

Once determined, k and ϕ_0 were substituted into the following equation from Allen and Allen (1990, p.270):

$$y'_2 - y'_1 = (y_2 - y_1) - \frac{1}{k} \cdot \ln \frac{\frac{1}{\phi_0} + ky_2}{\frac{1}{\phi_0} + ky_1} + \frac{1}{k} \cdot \ln \frac{\frac{1}{\phi_0} + ky'_2}{\frac{1}{\phi_0} + ky'_1} \quad (2)$$

(where $y'_2 - y'_1$ = decompacted sediment thickness from any time to the present, and $y_2 - y_1$ = sediment thickness given depths y_2 and y_1), which is solved by iteration.

Decompacted sedimentation rates were calculated between each pair of mbsf depth/age tie points and then linearly interpolated for sample points between these. The resulting values are recorded against the lower of each two points used for the calculation in Table 2. Decompacted sedimentation rates so determined range from less than 50 m/m.y. (419 mbsf, Hole 977A; 2 mbsf, Hole 979A) to in excess of 1000 m/m.y. (470–490 mbsf, Hole 979A).

RESULTS

Sediment Texture

A modified form of the ternary classification scheme used by Comas, Zahn, Klaus, et al. (1996, fig. 5) is used to classify sediments in this study. The modification was necessitated by the sieve sizes employed. In Figure 8, this modification has the effect of "moving" data points towards the clay and fine silt (top) apex, parallel to the tie line between clay and fine silt and medium and coarse silt. Figure 8 confirms the visual description made by the shipboard scientists and, given the above, that the dominant textural lithology in lithostratigraphic Unit I throughout the Alboran Basin is clay and silty clay. Downhole distribution of sand (>63 µm), medium and coarse silt (63–32 µm +

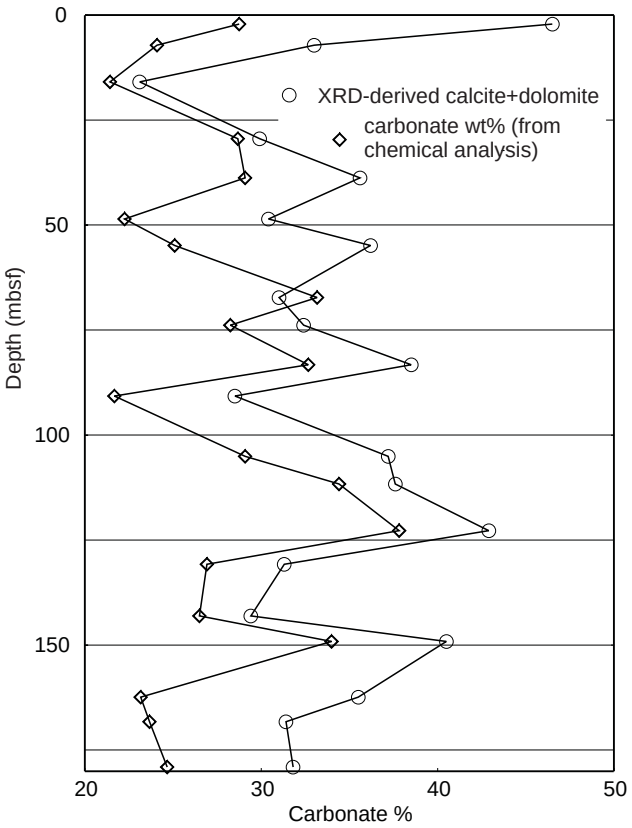

Figure 6. Downhole plot of chemically determined total carbonate content (wt%) and XRD calcite + dolomite data calculated using SIROQUANT for the uppermost 20 samples from Hole 976B (see Table 2 for sample numbers).

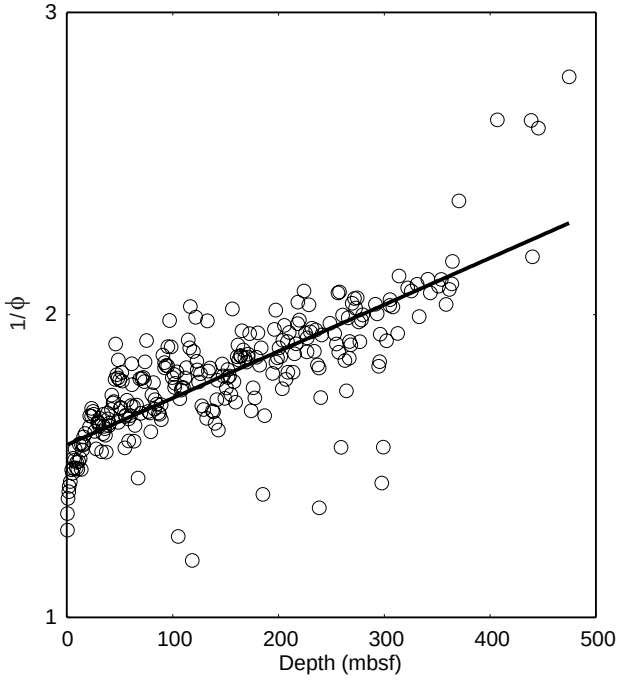

Figure 7. Cross plot of 1/ϕ against depth (mbsf) for Hole 976B, using physical properties data from Shipboard Scientific Party (1996b, fig. 124). Equation of linear regression 1/ϕ = 0.00154605 × depth + 1.56987; correlation coefficient = 0.59812.

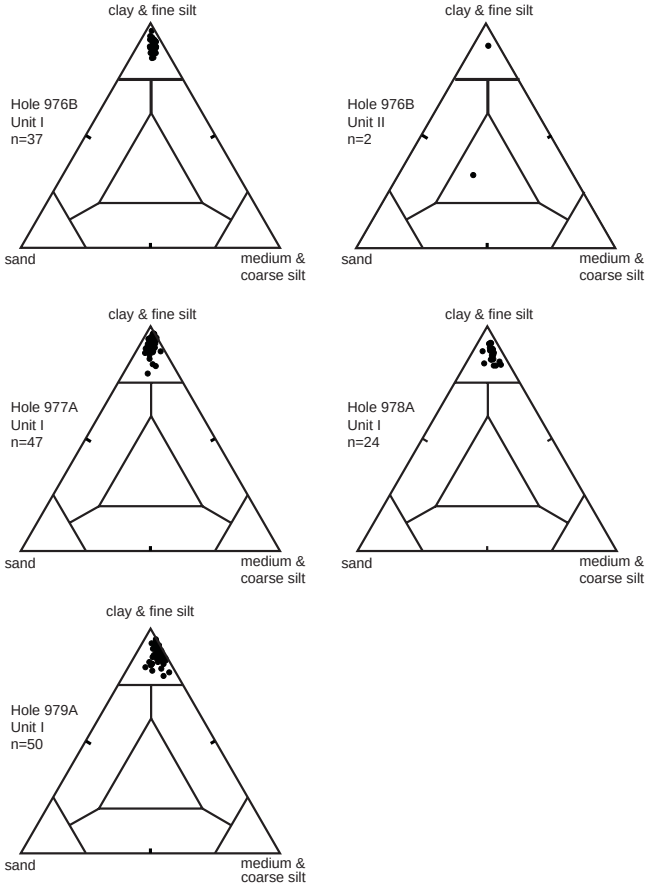

Figure 8. Ternary plots of sediment texture for the Alboran Sea sites. Note that the apices are modified from Comas, Zahn, Klaus, et al. (1996, fig. 5); sand = >63-µm fraction, medium and coarse silt = 63- to 20-µm fractions, clay and fine silt = <20-µm fraction.

32–20 µm), and fine silt and clay (<20 µm) is shown in Figure 9. The average and standard deviation for sand content is 4.1% ± 1.5% (Hole 976B), 4.0% ± 2.5% (Hole 977A), 4.4% ± 1.7% (Hole 978A), and 3.2% ± 2.4% (Hole 979A). For the medium and coarse silt fractions, these measures are 6.0% ± 1.6% (Hole 976B), 4.3% ± 2.% (Hole 977A), 8.0% ± 2.5% (Hole 978A), and 8.7% ± 2.7% (Hole 979A), and for clay and fine silt, they are 89.9% ± 2.8% (Hole 976B), 91.7% ± 3.9% (Hole 977A), 87.7% ± 3.1% (Hole 978A), and 88.1% ± 3.7% (Hole 979A). These data show a consistent downhole distribution of the textural components in Unit I in all four holes. No between-hole correlatable trends could be discerned.

XRD Mineral Quantification

XRD data were collected for each unsorted sample and for each of the four grain-size splits for each sample giving a total of 800 analyses. In addition, two repeats were run for unsorted samples (Samples 161-976B-1H-2, 64–68 cm, and 161-977A-1H-3, 53–57 cm) to check duplication of results, and blanks were run on the glass slides and plastic sample holders used during data collection. Normally, SIROQUANT quantification was performed twice on each sample, to check duplication on the unsorted, >63-µm, and <20-µm fractions, and in each case, the value derived from the second SIROQUANT analysis is reported, where these values fell within the error range reported for the first run. Otherwise, the analysis was rerun until two succeeding runs fulfilled this criterion. Because of time constraints, the 63- to 32-µm and 32- to 20-µm fractions were not analyzed using SIROQUANT. Again, this did not compromise the study, which was principally aimed at examining detrital mineral distribution in the sand and clay fractions.

Percentages for each of the minerals in the suite described above in the unsorted, >63-µm, and <20-µm fractions are given in Table 2, together with χ^2 values for each analysis.

Downhole Mineral Trends

Downhole trends for quartz, “clay” (chlorite + illite + kaolinite + muscovite + talc), and total carbonate (dolomite + calcite) are shown in Figure 9. These values, with the addition of total feldspar (albite + bytownite + orthoclase), have been normalized after removal of authigenic pyrite, halite, and gypsum. For comparison, the original shipboard estimates of quartz + feldspar + rock fragments + mica (QFRM) have also been plotted on Figure 9 (column 2) for each hole. As the latter values were calculated from different samples to those used in the study reported here, they give a reasonable indication of downhole trends that is independent of sample location, and, therefore, provides an independent check for the data. Comparison of the original shipboard data with the quartz XRD data for Hole 976B shows that the trends seen in the former broadly correlate with the XRD-derived data in the upper half of the hole (peaks in both data sets at around 10, 50, and broadly from 130 to 170 mbsf), but cannot be matched in lithostratigraphic Unit I below 220 mbsf. No similar correlations exist for Holes 977A, 978A, or 979A, most probably reflecting large errors associated with visual estimation.

The “clay” group is considered to include both authigenic material (precipitated, and directly from the breakdown of feldspar and rock fragments) as well as detrital material, principally muscovite. These phyllosilicates have not been considered separately because SIROQUANT had difficulty in modeling their variable compositions using pure muscovite and talc hkl files. Similarly, the feldspar group has not been included because an unknown proportion of original detrital material has broken down into clay. For these reasons, only quartz has been used as an indication of detrital input.

Inspection of Figure 9 shows no consistent downhole trends for any of the mineral components in unsorted samples or in any of the grain-size splits, except for an inverse relationship between total carbonate, most commonly the dominant component, and either quartz and/or total “clay.” One example of this inconsistent variability is seen in the total carbonate plots for the unsorted samples (Fig. 9, column 2). In this case values decrease downhole in Holes 976B, 977A, and 978A, but are more or less constant downhole in 979A. Similar inconsistent trends occur for all other components. Statistics have not been calculated for the individual mineral components because the data are not considered absolute as discussed earlier.

Between-Hole Correlations

The only obvious variation in the bulk mineralogy of lithostratigraphic Unit I between holes is the direct relationship between water depth and >63-µm-fraction carbonate content. The highest sand-sized carbonate content (and correspondingly lowest quartz content) occurs in Holes 977A and 978A, both of which lie beneath almost 2000 m of water (Fig. 9, column 3), whereas the overall carbonate content is much lower in Holes 976B and 979A, both of which lie in just over 1000 m of water.

More interesting findings result from an examination of various mineralogical parameters and sedimentation rates between holes. These correlations are given in Figures 10 through 13. All between-hole correlations were undertaken using a downhole time scale in preference to depth to facilitate direct comparison and highlight temporal synchroneity. As this time scale is a derivative of depth (see above), it is subject to precision and accuracy errors in the resolution

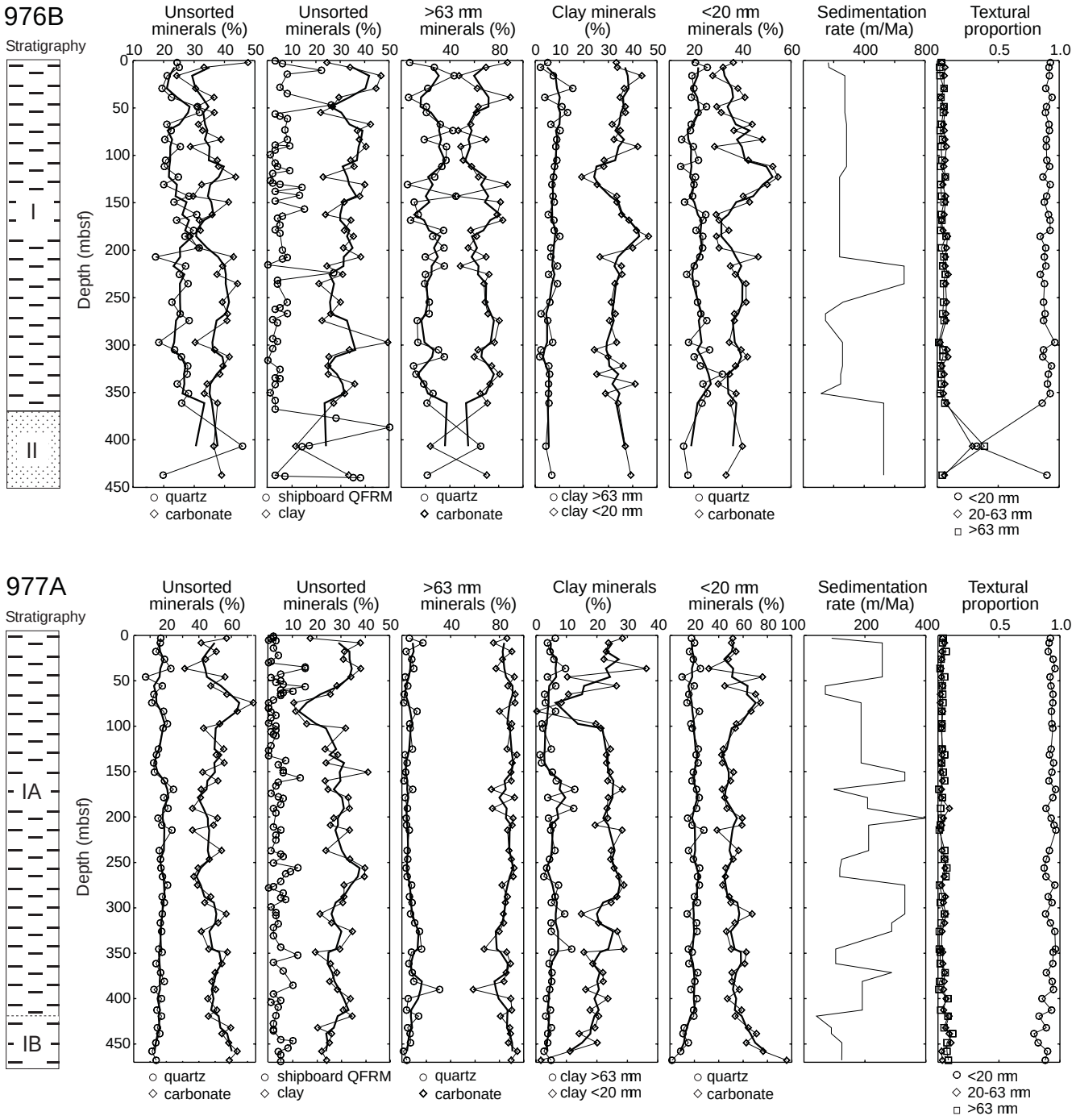

Figure 9. Downhole plots of decompacted sedimentation rate; shipboard estimate of quartz + feldspar + rock fragments + mica (QFRM), unsorted quartz, carbonate, total "clay"; >63-µm quartz, carbonate, total "clay," <20-µm quartz, carbonate, total "clay"; and textural sand (>63 µm), coarse and medium silt (20–63 µm), and fine silt and clay (<20 µm) for Holes 976B, 977A, 978A., and 979A. Thin lines and symbols represent actual data; thick lines are three-point moving averages. (Continued next page.)

of the age determinations, and so exact time correlations cannot be expected. The correlations indicated on Figures 10 through 12 were undertaken by visual matching of peaks in the smoothed downhole data only where these are defined by more than one point.

Figures 10, 11, and 12 show cross-hole correlations for unsorted, >63-µm, and <20-µm fractions for the components quartz, carbonate (dolomite + calcite), and quartz normalized against "clay" and feldspar, after the removal of dolomite, calcite, pyrite, gypsum, and halite (hereafter referred to as normalized quartz). The latter parameter was calculated to remove the dominating effect of pelagic carbonate to see if any underlying trends were apparent in the remaining components, principally the quartz. Curves so derived show that there are no clear basin-wide correlatable trends in the distribution of sand-sized quartz—apparent correlation in unsorted and >63-µm fractions is believed to be a partial artifact of much stronger carbonate correlations, which are described below. The good correlation of cycles of quartz

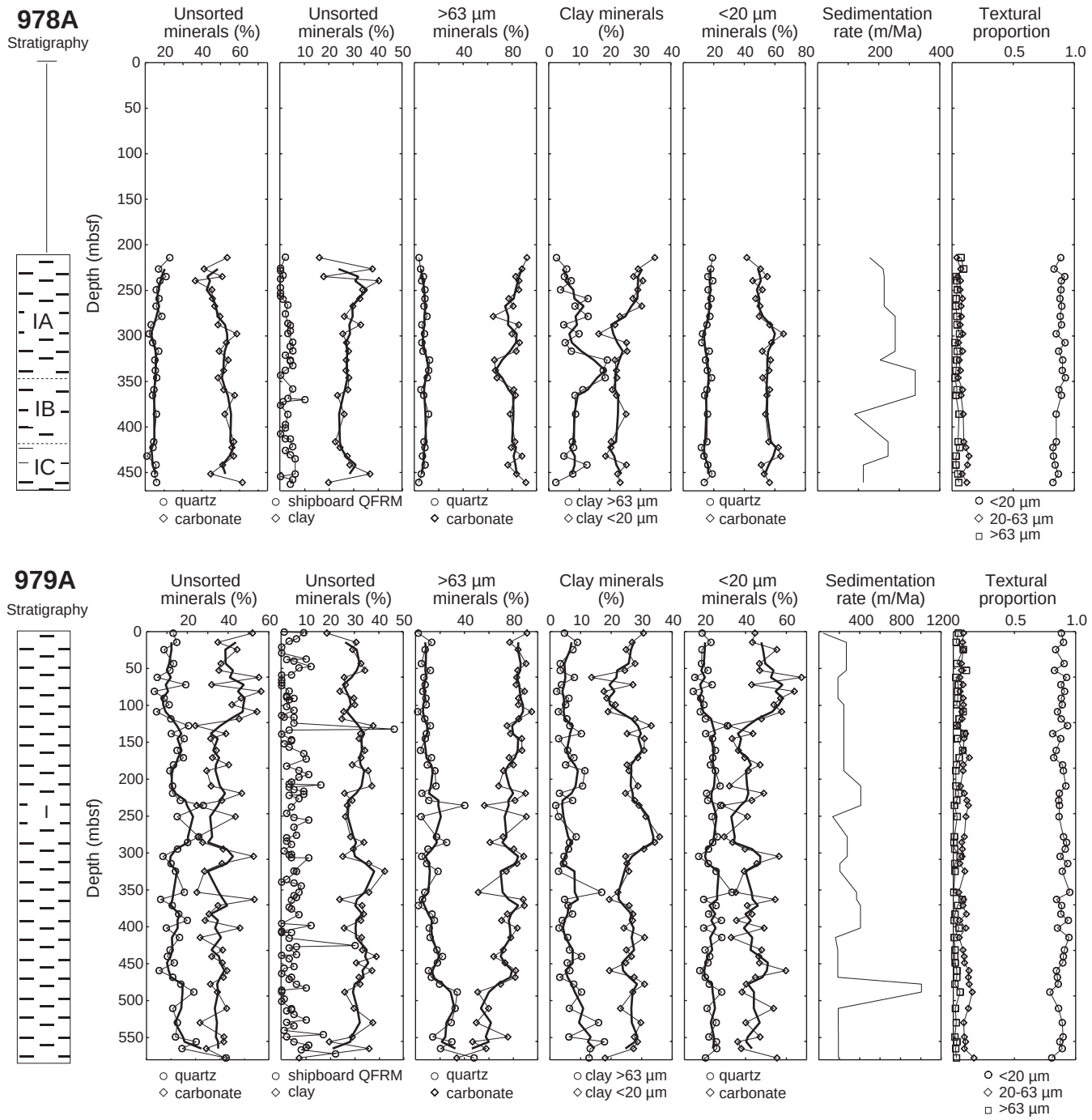

Figure 9 (continued).

distribution in the <20-µm fraction seen in the upper graph of Figure 12 is almost certainly attributable to the good correlation in the dominant carbonate fraction (Fig. 12, <20-µm carbonate), as all but the coincidence at ~0.5 Ma disappear after carbonate is removed (Fig. 12, <20-µm quartz).

In contrast, there is a reasonably strong basin-wide correlation in carbonate distribution between the sites, particularly for the <20-µm fraction. Correlation is least clear in the unsorted fraction (Fig. 10), probably because more obvious temporal correlations in the >63-µm (Fig. 11) and <20-µm (Fig. 12) fractions are not synchronous with each other. The frequency of cyclicity in the >63-µm fraction is ~0.75 m.y., whereas strongly correlated cycles in the <20-µm samples have regularly repeated every 0.5 m.y. since ~2.5 Ma.

Sedimentation rates across the basin are broadly correlated as indicated on Figure 13, although this is less convincing than the carbonate data. Between 1.0 and 2.0 Ma, peaks in the <20-µm carbonate cycles seem to correspond with sedimentation-rate highs, except at Site 978, but no such coincidence is observed in sediments younger and older than this. There is a moderately well-defined correlatable quartz peak in both the >63-µm and <20-µm data at around 2.6–2.7 Ma that coincides with the poorly defined sedimentation-rate high at that time. However, the sedimentation-rate high from 100 to 300 ka

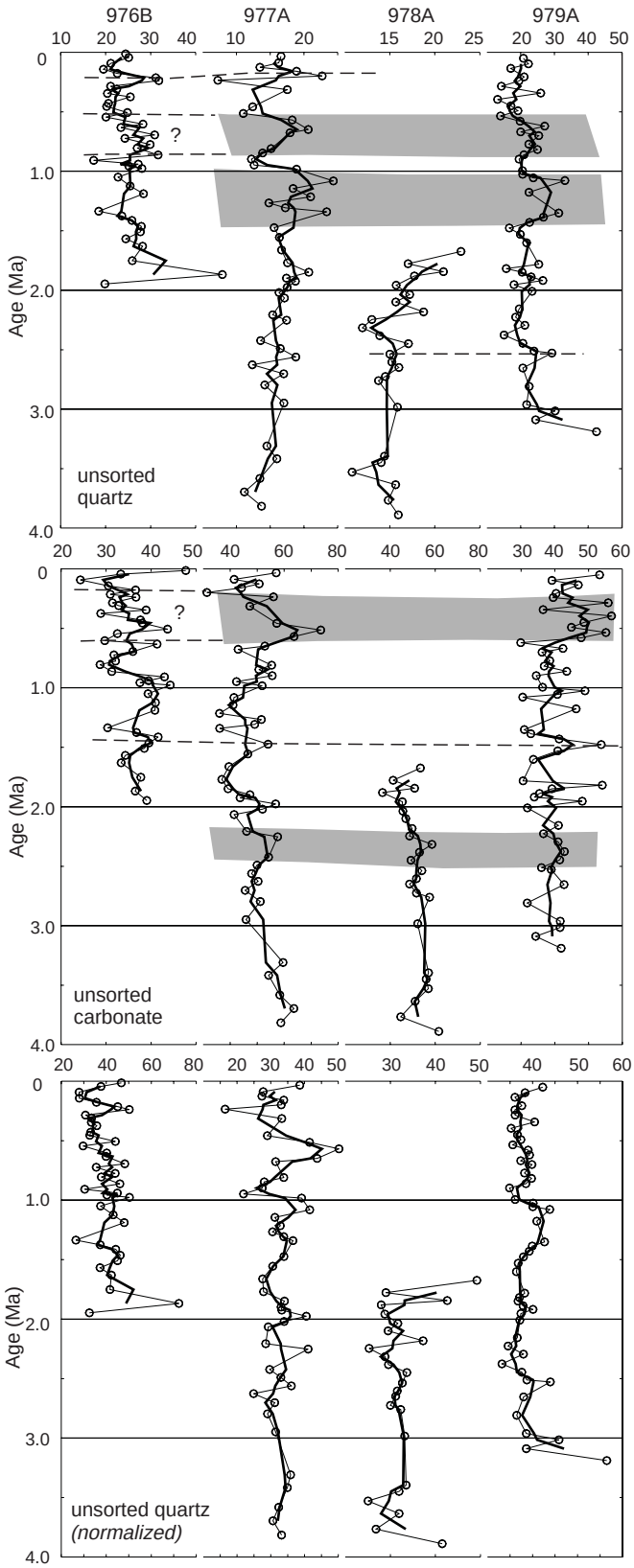

Figure 10. Between-hole correlation of quartz (top), carbonate (middle), and carbonate-normalized quartz (bottom) for unsorted samples. Thin downhole lines and symbols represent actual data; thick lines are three-point moving averages. Correlations discussed in text are shown by shading; ? = tentative correlation.

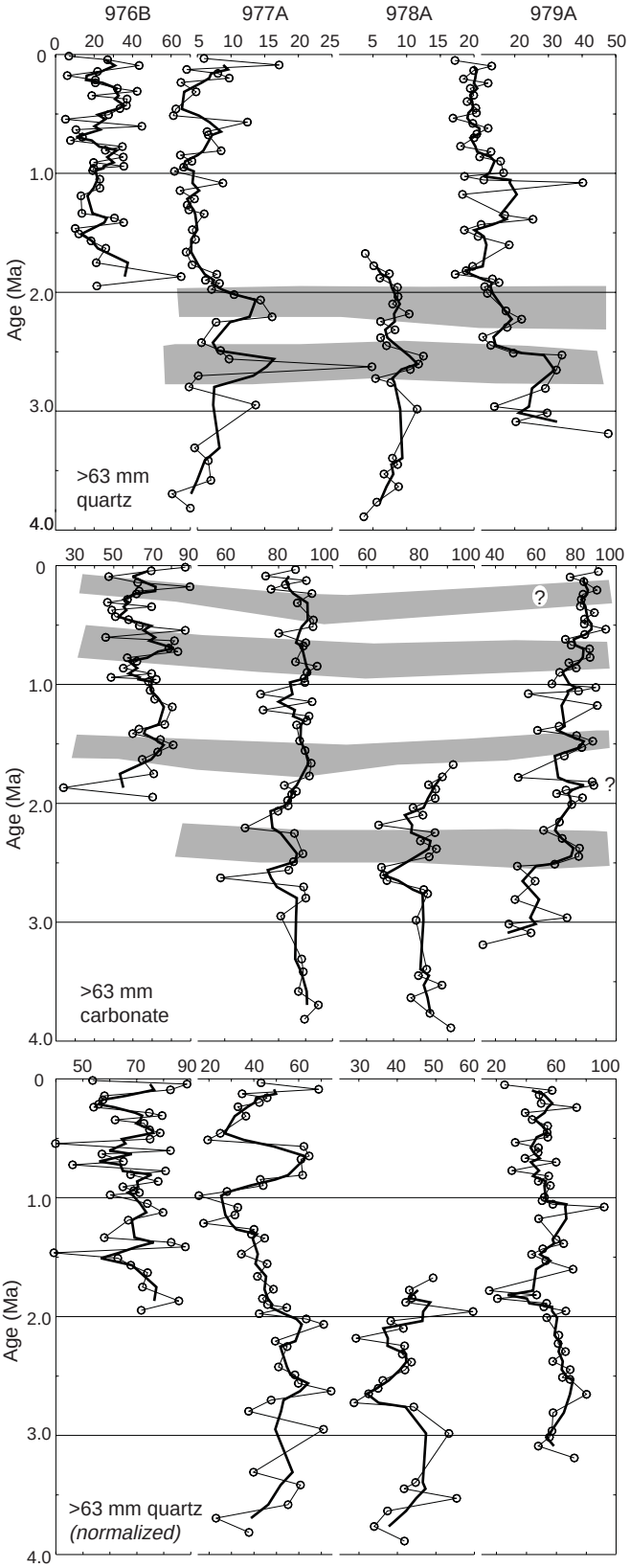

Figure 11. Between-hole correlation of quartz (top), carbonate (middle), and carbonate-normalized quartz (bottom) for >63-µm samples. Thin downhole lines and symbols represent actual data; thick lines are three-point moving averages. Correlations discussed in text are shown by shading; ? = tentative correlation.

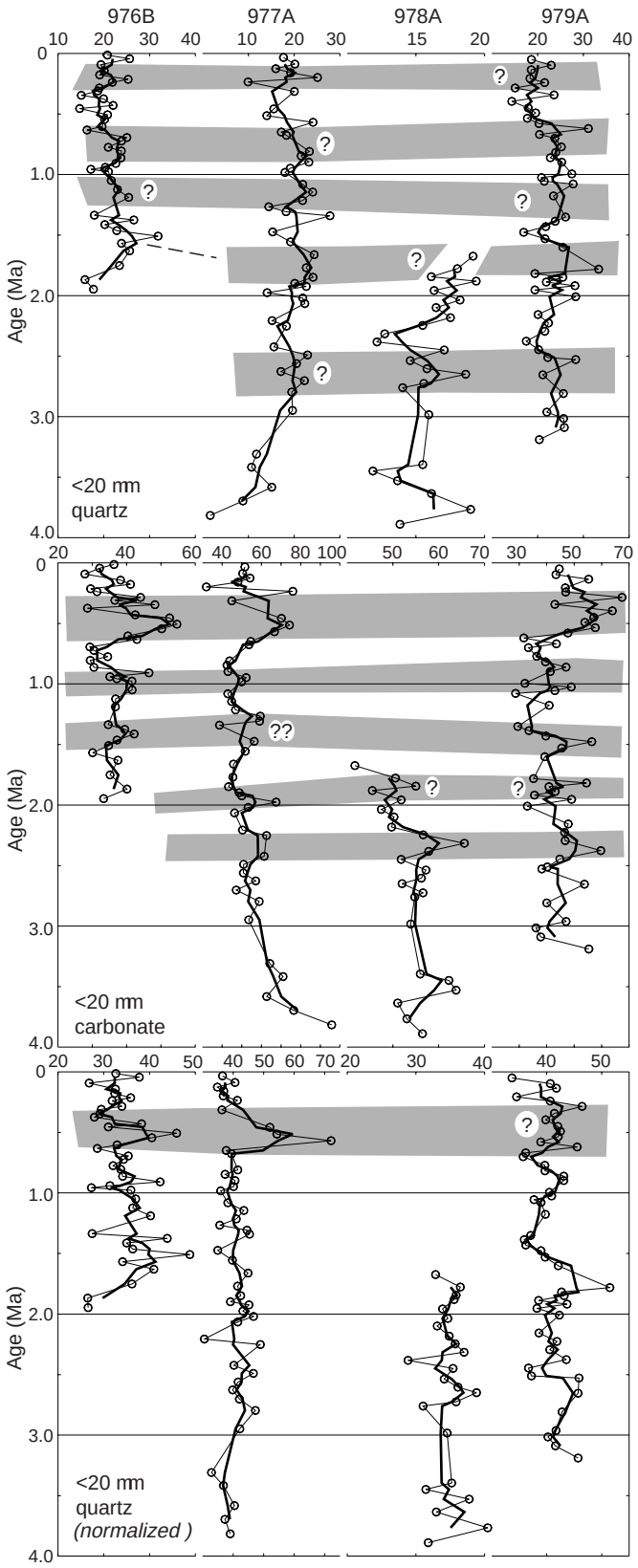

Figure 12. Between-hole correlation of quartz (top), carbonate (middle), and carbonate-normalized quartz (bottom) for <20-µm samples. Thin downhole lines and symbols represent actual data; thick lines are three-point moving averages. Correlations discussed in text are shown by shading; ? = tentative correlation.

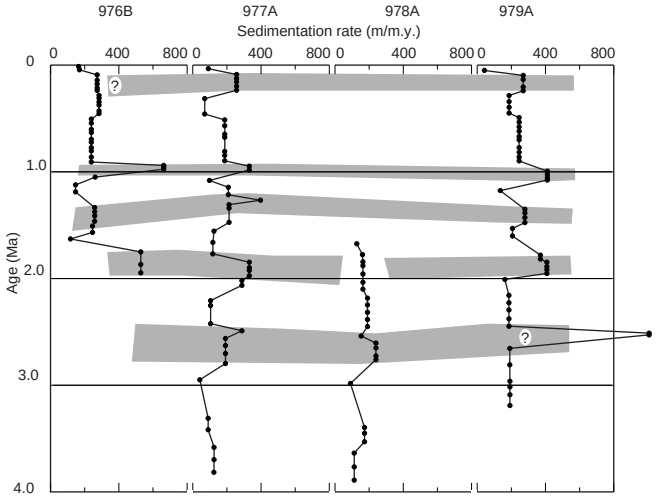

Figure 13. Cross-hole correlation of decompacted sedimentation rate; ? = tentative correlation.

corresponds with upward decreasing carbonate, particularly in the <20-µm fraction, and highly variable quartz content.

SEM Analysis

SEM examination of selected samples confirmed shipboard determinations that the principal carbonate component of the sand (>63-µm) fraction is foraminifer tests, whereas the dominant carbonate component of the <20-µm fraction is calcareous nannofossils, but with fragments of foraminifer tests also present (Fig. 14). In addition, rounded to subrounded quartz is present in both the >63-µm and <20-µm fractions, with rounded to subhedral feldspar additionally present in the <20-µm fraction. This is interpreted to indicate the presence of detrital quartz in both the >63-µm and <20-µm fractions.

DISCUSSION

Given the present deep open marine setting of the holes drilled during Leg 161 and the likelihood that similar conditions have existed throughout the late Pliocene–Holocene (as indicated by the similarity of the fossil assemblage and lithology throughout the sequence), three possible interpretations can be used to explain the paucity of primary sedimentary structures, poor sorting, abundance of trace fossils, and the mixed siliciclastic/carbonate provenance of most of the sediment. They are dependent in part on the grain size of the detrital siliciclastic material. These scenarios, discussed further later in this paper, are the following:

1. Siliciclastic sediment was transported into the basin by bottom-flowing currents (e.g., low-density turbidity currents), deposited as discrete beds, and subsequently mixed with the pelagic and hemipelagic material by biological action. In this case, the clastic material would be sand or coarse to medium silt grade.
2. Siliciclastic material was emplaced as poorly sorted, mass-flow deposits that were subsequently bioturbated, where a grain-size distribution similar to that in the first scenario would be expected.
3. Siliciclastic material forms part of the hemipelagic rain that was transported either in suspension or by wind, and was deposited with no inherent grain-size segregation so that subsequent bioturbation simply churned an already homogenous mix. In the latter case, a wide range of grain sizes would be expected, but with fine silt and clay dominant.

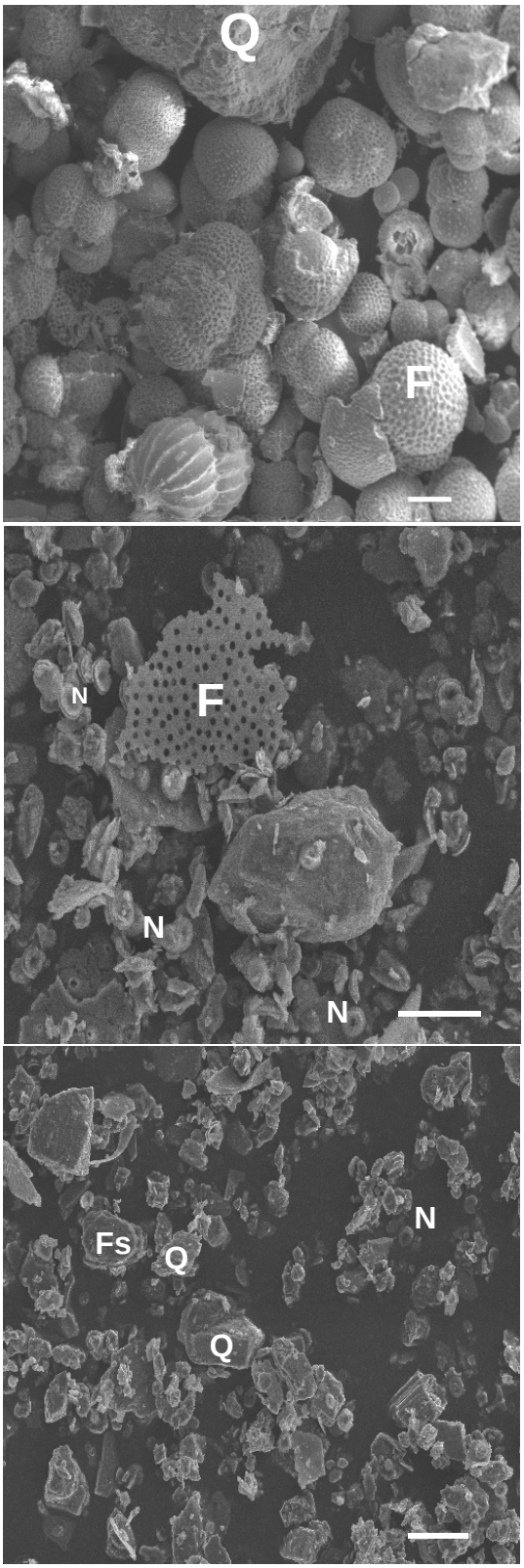

Figure 14. SEM images of sediment splits. **Top:** Sample 161-976B-15X-3, 76–80 cm, >63-µm split; bar scale = 100 µm, accelerating voltage = 15 kv. **Center:** Sample 161-976B-15X-3, 76–80 cm, <20-µm split; bar scale = 10 µm, accelerating voltage = 8 kv. **Bottom:** Sample 161-976B-20X-3, 95–100 cm, <20-µm split; bar scale = 10 µm, accelerating voltage = 8 kv; Q = quartz, N = calcareous nannofossil, F = foraminifer, Fs = feldspar.

One unexpected result of this study is the possibility of climatic cycles being represented by variation in the sedimentary section. The presence of diffuse ORLs in the Alboran Basin, many of which can be correlated with more characteristic sapropels (sensu Hilgen, 1991) further to the east (see Murat, Chap. 41, this volume), suggests that climate/ocean circulation cyclicity has affected part of the sedimentary record (i.e., the organic content) in the past, at a frequency that is an order of magnitude greater for the ORLs than that discussed below for the carbonate sediments. The latter are mineralogically indistinguishable from sediments adjacent to the ORLs, which supports an argument for at least two levels of regional control operating in the basin.

Tectonic/Physiographic Location of Sites

Hole 976B was drilled on a basement high, but seismic data (Shipboard Scientific Party, 1996b, figs 3 and 4) show the upper Pliocene–Pleistocene section to thicken toward the southeast, in the direction of the current depocenter of the West Alboran sub-basin. In other words, during the late Pliocene to Holocene, Site 976 was located at a zone of marine slope deposition, rather than at the base of the slope. The location is physiographically separated from the South (Site 979) and from the East (Sites 977 and 978) Alboran sub-basins by the northeast-trending volcanic Alboran Ridge (Fig. 1).

Sites 977 and 978 are located with the East Alboran Basin, near the center of two east-dipping in-filled submarine depressions, to the south and north of the Al-Mansour Seamount, respectively. The seamount is a prominent bathymetric high, which could have influenced the nature and distribution of sedimentation throughout the late Pliocene–Holocene. Site 979 is located on the southeastern flank of the Alboran Ridge, and from late Pliocene to Holocene times, it has been located near the distal end of a deep submarine ramp (Shipboard Scientific Party, 1996e, figs. 3 and 4).

The Al-Mansour Seamount and the Alboran Ridge are believed to have formed during the early Miocene (Comas et al., 1992; Woodside and Maldonado, 1992) during a period of extension that continued into the late Miocene (Watts et al., 1993). Both the volcanics and adjacent Miocene sediments have undergone compressional structural modification since then (Shipboard Scientific Party, 1996e). The four sites occupied during Leg 161 provided widely spaced coverage of the main physiographic provinces of the Alboran Basin, some of which have been isolated from each other throughout the late Pliocene–Holocene. One result of this is that correlatable sedimentation events must invoke regional control mechanisms rather than site-specific ones in their explanation.

The four sites represent a variety of deep marine depositional environments including slope, ramp, and basin depocenter settings, and the minor lithologies present at each site may represent these differences. For example, slumping is more common in the depocenter settings represented by Holes 977A and 978A.

Sedimentary Indicators of Siliciclastic Depositional Environment

Graded beds of sand and coarse silt (lithostratigraphic Unit II, Hole 976B; lithostratigraphic Subunit IA, Hole 978A; Unit I, Hole 979A), packstone (Hole 978A, Subunit IA), and mass-flow units, including slumps and breccias (Subunits IA and IB, Hole 977A; Subunit IC, Hole 978A), all suggest that both gravity currents and mass-flow mechanisms have been operating in the basin throughout the last 4 m.y.

The presence of sand-sized quartz throughout the sequence in all holes necessitates transport by sediment gravity currents, either to the site of original deposition (in the case of mass-flow emplaced units) or at the current locations of the drill holes. Localized gravity flows are further supported by the lack of regional correlation between quartz cycles (Figs. 10–12).

The trace-fossil assemblage comprising mainly *Zoophycus* and *Chondrites* ichnogenera and belonging to the Zoophycus to Nereites associations (Collinson and Thompson, 1982, fig. 9.41) also supports a deep marine depositional setting for both the sandy and finer material. Graded sand and coarse silt beds 2–10 cm thick are uncommonly present in the sequence. If these are representative of average deposition of material of this grade, then it is likely that the benthic fauna would have little difficulty in reworking and homogenizing this material into the hemipelagic sediment, especially if the turbidite events are relatively infrequent as is suggested by the overall low percentage of sand and coarse silt in the sequence (everywhere <10%). In contrast, mass-flow units of thickness exceeding 1 m are unlikely to be completely reworked, and so their relative paucity suggests a low frequency of occurrence. None of the sand material comprising lithostratigraphic Unit I is considered to have been deposited as part of base-of-slope or inner (upper) fan complexes because of the lack of thick, coarse-grained units. Even in Unit II, Hole 976B, sand beds appear to have been of similar dimension to those preserved rarely in Unit I, the principal difference being their more common occurrence.

At this stage it is not possible to support the contention of shipboard scientists (Shipboard Scientific Party, 1996b, fig. 25) about cycles of upward increasing detrital content being present in Unit I at Site 976. It is more likely that the sand- and coarse silt-sized sediment recovered from the sites represents deposition onto the deep marine basin floor into which the distal parts of infrequent gravity currents flowed.

The origin of fine silt- and clay-sized detrital quartz (together with feldspar and presumably muscovite) is more equivocal. This material could easily have been incorporated in localized turbidity current flows as part of the grain-size continuum. However, the possible correlation of <20-µm quartz cycle peaks between 2 and 3 Ma (Fig. 12) points to a regional control that may be climatic in origin. Possibilities include (1) that the cycles relate to arid periods occurring on the north Africa continent and a resultant increase in eolian transport, or (2) fluctuations in atmospheric circulation causing changes in prevailing wind direction (Moulin et al., 1997).

Carbonate Cycle Synchroneity

The 9-m spacing of samples (~1 per core) has been sufficient to define a basin-wide correlation of carbonate cycle peaks on a frequency of ~500 ka for the distribution of calcareous nannofossils, and this suggests a control mechanism that is at least of regional extent. The fact that similar synchroneity is not present in the detrital (quartz) distribution indicates the control is probably not a tectonic one. Cycles of this order of magnitude (~400 ka) fall at the upper end of fourth- and fifth-order sea-level cycles (Fischer, 1986) and, hence, have been interpreted to result from climatic variation associated with Milankovitch orbital cycles (Cotillon, 1991). Similar periodicities were reported by Moore et al. (1982) for upper Miocene and Quaternary deep marine carbonate sediments in the Pacific Ocean. In that example, the variation is attributed to changes in the carbonate compensation depth brought about by climatic factors. In the Alboran Sea, climate appears to have affected microfossil abundance rather than preservation. The fact that cycles in the >63-µm carbonate fraction (mainly foraminifers) do not appear to be synchronous with those in the <20-µm carbonate fraction (mainly nannofossils) suggests that the climatic effect may also be species selective.

CONCLUSIONS

Deep marine sediment in the Alboran Basin, as represented by samples collected from Sites 976, 977, 978, and 979, is remarkably homogeneous throughout the upper Pliocene to Holocene section. Most is structureless to burrowed clay and silty clay in which calcareous nannofossils are the principal component, with subordinate sand-sized foraminifers.

Throughout the sequence quartz and feldspar are minor but persistent components, generally making up less than 10%. Grains range in size from sand to clay, and at least in the case of quartz, they are detritally derived as evidenced by the coarser grain sizes and rounding seen on SEM images. The detrital input to the basin, represented by the quartz and feldspar fractions in the holes, appears to have been controlled by local sedimentation events such as immediate source and short-lived restricted bottom-flowing currents, rather than by regional ones. The main evidence for this is the lack of correlation between cycles in the quartz distributions. Given the proximity and elevation of the adjacent tectonic hinterland, it was hypothesized that regional tectonic events may have been reflected in detrital input that could be regionally correlated,; however there is no discernible evidence of such events. Variation is either not detectable at the sampling scale used, or the events did not occur.

There is no evidence to support the contention of shipboard scientists (Shipboard Scientific Party, 1996b) that the detrital input represented by quartz + feldspar + rock fragments + mica (QFRM) in Hole 976B was arranged into upward-increasing cycles, each ~150 m thick (similar to the thickness of the turbidite channel fill represented by lithostratigraphic Unit II at Site 976). Overall, detrital sediments compose less than 10% of the sediment and are interpreted to be biologically mixed, relatively thin, distal turbidite deposits. This is not to say that submarine fans or base-of-slope aprons do not exist in the Alboran Basin, only that none were intersected by holes drilled during Leg 161, with the exception of Unit II at Site 976. On the basis of seismic evidence and the presence of an erosional base, this sequence appears to be a localized channel-fill deposit located on the northern slope of the Western Alboran sub-basin. The lack of coarse-grained deposits at other sites in the upper Pliocene to Holocene is not surprising given the physiographic locations of the drilling sites.

A regional correlation exists in cycles based on the proportion of carbonate, and these can be separated into <20-µm (mainly calcareous nannofossils) and >63-µm (mainly foraminifer) fractions. In the former, cycles have a frequency of occurrence of ~500 k.y., whereas in the latter, which are less well defined, the repetition rate is ~750 k.y. Both can be equated with fourth- to fifth-order sea-level cycles and are attributed to climatic control, most likely caused by orbital eccentricity variability.

ACKNOWLEDGMENTS

We would like to acknowledge Timothy Sharp, John Allen, and Mark Tindale for their assistance with laboratory analysis and preparation of XRD samples. Maree Anast contributed greatly to the acquisition and interpretation of the XRD data, and, particularly, aided with the use of SIROQUANT. Rick Wuhrer collected the SEM images. The manuscript has benefited from the input of Adrian Cramp and Cristino Dabrio. The work was supported by UTS internal research grant no. 0681r.

REFERENCES

Allen, P.A., and Allen, J.R., 1990. *Basin Analysis: Principles and Applications:* Oxford (Blackwell Sci. Publ.).

Collinson, J.D., and Thompson, D.B., 1982. *Sedimentary Structures:* London (George Allen and Unwin).

Comas, M.C., García-Dueñas, V., and Jurado, M.J., 1992. Neogene tectonic evolution of the Alboran Basin from MCS data. *Geo-Mar. Lett.,* 12:157–164.

Comas, M.C., Zahn, R., Klaus, A., et al., 1996. *Proc. ODP, Init. Repts.,* 161: College Station, TX (Ocean Drilling Program).

Cotillon, P., 1991. Varves, beds and bundles in pelagic sequences and their correlation (Mesozoic of SE France and Atlantic). *In* Einsele, G., Ricken,

W., and Seilacher, A. (Eds)., *Cycles and Events in Stratigraphy:* Berlin (Springer-Verlag), 820–839.

Falvey, D.A., and Middleton, M.F., 1981. Passive continental margins: evidence for a prebreakup deep crustal metamorphic subsidence mechanism. In *Colloquium on Continental Margins (C3, Paris, 7*–17, July 1980). Oceanol. Acta, 4 (Suppl.):103–114.

Fischer, A.G., 1986. Climatic rhythms recorded in strata. *Annu. Rev. Earth Planet. Sci.,* 14:351–376.

Hilgen, F.J., 1991. Astronomical calibration of Gauss to Matuyama sapropels in the Mediterranean and implication for the geomagnetic polarity time scale. *Earth Planet. Sci. Lett.,* 104:226–244.

Moore, T.C., Jr., Pisias, N.G., and Dunn, D.A., 1982. Carbonate time series of the Quaternary and late Miocene sediments in the Pacific Ocean: a spectral comparison. *Mar. Geol.,* 46:217–233.

Moulin, C., Lambert, C.E., Dulca, F., and Dayan, U., 1997. Control of atmospheric export of dust from North Africa by the North Atlantic Oscillation. *Nature,* 387:691–694.

Shipboard Scientific Party, 1996a. Explanatory notes. *In* Comas, M.C., Zahn, R., Klaus, A., et al., *Proc. ODP, Init. Repts.,* 161: College Station, TX (Ocean Drilling Program), 21–49.

————, 1996b. Site 976. *In* Comas, M.C., Zahn, R., Klaus, A., et al., *Proc. ODP, Init. Repts.,* 161: College Station, TX (Ocean Drilling Program), 179–297.

————, 1996c. Site 977. *In* Comas, M.C., Zahn, R., Klaus, A., et al., *Proc. ODP, Init. Repts.,* 161: College Station, TX (Ocean Drilling Program), 299–353.

————, 1996d. Site 978. *In* Comas, M.C., Zahn, R., Klaus, A., et al., *Proc. ODP, Init. Repts.,* 161: College Station, TX (Ocean Drilling Program), 355–388.

————, 1996e. Site 979. *In* Comas, M.C., Zahn, R., Klaus, A., et al., *Proc. ODP, Init. Repts.,* 161: College Station, TX (Ocean Drilling Program), 389–426.

Skilbeck, C.G., Cornell, W., Fukusawa, H., Ippach, P., Marsaglia, K., Murat, A., and Tribble, J.S., 1995. Patterns of cyclic sedimentation in the Alboran Basin (western Mediterranean Sea): correlation and relationship to sedimentation rate. *Eos,* 76:F624.

Stanley, D.J., Kelling, G., Vera, J.-A., and Sheng, H., 1975. Sands in the Alboran Sea: a model for input in a deep marine basin. *Smithsonian Contrib. Earth Sci.,* 15.

Watts, A.B., Platt, J.P., and Bulh, P., 1993. Tectonic evolution of the Alboran Sea Basin. *Basin Res.,* 5:153–177.

Woodside, J.M., and Maldonado, A., 1992. Styles of compressional neotectonics in the Eastern Alboran Sea. *Geo-Mar. Lett.,* 12:111–116.

Date of initial receipt: 27 May 1997
Date of acceptance: 2 December 1997
Ms 161SR-210